Force-matched empirical potential for martensitic transitions and plastic deformation in Ti-Nb alloys

Robert C. Ehemann and John W. Wilkins

Phys. Rev. B **96**, 184105 — Published 10 November 2017

DOI: 10.1103/PhysRevB.96.184105

Force-matched empirical potential for martensitic transitions and plastic deformation in Ti-Nb alloys

Robert C. Ehemann and John W. Wilkins
Department of Physics, The Ohio State University, Columbus, Ohio 43210, USA
(Dated: October 10, 2017)

A force-matched spline-based empirical potential based on the modified embedded-atom method is fit to an extensive database of highly-converged density functional theory calculations for titanium-niobium alloys with an evolutionary algorithm. Consistency with experiment and existing models is verified through calculations of structural, elastic and thermal properties. The potential is used to study the effects of alloying on elastic properties, the martensite phase of Ti-rich alloys and the α-β and β-ω transformations. Stress- and temperature-induced martensitic transitions are demonstrated in Ti-25 at.%Nb by NPT simulation. Last, the effect of alloying on screw dislocations in hcp-Ti and bcc-Nb is analyzed at 5 at.% solute content with the fitted potential.

PACS numbers: 34.20.Cf, 61.43.Bn, 81.30.Kf, 61.72.Ff
Keywords: titanium, niobium, alloy, interatomic potentials, martensitic transformations, dislocations

I. INTRODUCTION

Titanium is an important material in many modern industries. When alloyed with bcc-stabilizing elements (so-called β alloys), the bcc β phase can be stabilized at room temperature. One class of β alloys which has garnered much attention is "gum metals," which contain about 25 at.% of a primary β stabilizer and small amounts of other elements, e.g. Ta, Zr and O. These alloys have exceptional yield strength, high ductility and low elastic modulus[1], and exhibit superelasticity[1–5], shape memory[3,6] as well as martensitic[7,8] and strain-glass[9] transitions. The plastic deformation behavior of gum metals has been explored with great interest in order to explain these mechanical properties. Proposed mechanisms include dislocation-free deformation[1,10], stress-induced martensitic transitions[8,11,12], deformation twinning[11,12] and conventional dislocation-driven plasticity[13,14].

Niobium is commonly used as the major β-stabilizer in gum metals, and Ti-Nb alloys on their own show promise in biomedical[15–17] and orthodontic[18] applications, and are used as superconducting wires for electromagnets in MRI machines, synchrotrons and tokamaks. In the present work we develop a classical interatomic potential for Ti-Nb alloys with focus on properties of the gum metal approximant Ti_3Nb.

Classical molecular dynamics (MD) potentials, popular for their favorable scaling compared to first-principles methods, were traditionally developed by choosing analytic functional forms with a handful of free parameters determined by fitting directly to experimental bulk data such as cohesive energy, lattice, and elastic constants. The force-matching method of Ercolessi and Adams[19] has facilitated the development of interatomic potentials based on *ab initio* calculations of relaxed crystallographic defects, metastable structures, and other nonequilibrium configurations. Combined with spline-based parameterization of constituent functions first used by Lenosky *et al.*[20], this allows the development of empirical or semi-empirical interatomic potentials trained to large portions of the *ab initio* potential-energy landscape with minimal bias.

We present an empirical potential force-matched to a large database of *ab initio* forces, stresses and energies with an optimization scheme combining the Powell conjugate-direction[21] and genetic algorithms. Our model is an empirical extension of the modified embedded-atom method (MEAM)[22–26] for alloys, with functions parameterized by cubic splines. Section II describes the formulation of the model, the density functional theory (DFT) database, and the iterative process of fitting, testing, and database refinement. Section III contains calculations of structural, elastic and thermal properties to demonstrate accuracy of the fit and consistency with existing data. Section IV examines behavior of the fitted potential for martensitic transitions in pure titanium and Ti-rich alloys. Section V contains differential displacement maps of screw dislocation cores in hcp Ti and bcc Nb and examines the effect of alloying therein. Conclusions are given in Section VI.

II. OPTIMIZATION OF THE MEAM-LIKE EMPIRICAL POTENTIAL TO FIRST-PRINCIPLES DATA

Here we describe the DFT calculations from which we build the fitting database as well as the global optimization scheme employed.

A. Density-functional theory database

Highly converged DFT calculations performed with VASP[27–30] using a projector-augmented planewave basis[31] and Perdew-Burke-Erzenhof (PAW-PBE)[32,33] generalized-gradient exchange correlation approximation (GGA) comprise a database of forces, stresses and energies for fitting via the force-matching method of Er-

colessi and Adams[19]. Valence configurations are $3p4s3d$ and $4p5s4d$ for Ti and Nb pseudopotentials, respectively. Convergence with respect to planewave basis size, number of k-points for Brillouin zone integration, and 1^{st} order Methfessel-Paxton[34] smearing parameter is achieved to within 1 meV/atom for all structures in the fitting database. Chosen k-point grids are available in the Supplemental Material[35]. All electronic self-consistency loops are converged to 10^{-6}. Ionic relaxations are converged to 10^{-5}.

The fitting database contains 411 configurations with a total of 9,079 unique force components, stress components and energies to be fit. The potential contains 200 fitted parameters.

The remainder of this section describes the contents of the DFT database. In the first paragraph that follows we list structures for which points on the energy-volume curve at 50%, 97.5%, 100%, 102.5% and 120% equilibrium are included in the fitting database. In the second paragraph we list the structures for which elastic constants, calculated following the method of Trinkle[36], are included. In the third paragraph, given our interest in the martensitic transitions of this system, we describe structures along the transition pathways. In the fourth paragraph we list the various point and planar defect structures to which the potential is fit. The last two paragraphs in this subsection describe *ab initio* MD snapshots at finite temperature, each of which is run with a 1 fs timestep, and miscellaneous configurations which were added to correct for spurious results obtained with previous iterations of the potential. More detail on the iterative process of fitting, testing, and database refinement is provided Subsection II C.

The fitting database contains energy-volume relations for multiple phases at each considered stoichiometry, including those that are dynamically or elastically unstable, in order to broadly sample the configuration space and train the potential to non-equilibrium configurations. For pure titanium we include the hcp α, bcc β, hexagonal ω, fcc and A15 phases while for niobium we include bcc, hcp, ω-Ti, A15 (also known as β-W) and β-Ta phases. Since the solid-solution nature of alloys is impractical to account for within DFT, representative supercells for each phase must be used. Structure candidates for Ti_3Nb hexagonal α', orthorhombic α'', bcc (β) "$G1$" and hexagonal ω phases are taken from Lazar *et al.*[37], who performed a thorough analysis of their stability. Additionally, a 16-atom bcc special quasi-random structure (SQS)[38], the bcc $D0_3$ and $L6_0$ structures, the hcp $D0_{19}$ and the A15 structure are included for this stoichiometry. For TiNb, a [110]-layered bcc supercell (where [110] alternate between Ti and Nb, space group $Pmmm$), bcc B2 and hcp A3 structures are included. Finally a bcc SQS and an A15 $TiNb_3$ phase, which is predicted by DFT to be elastically and dynamically stable, are included in the database.

The fitting database contains elastic constants for hcp, bcc and ω phases of titanium; $D0_3$, $G1$, ω and α'' phases of Ti_3Nb; the $B2$ phase of TiNb and bcc niobium; each at ± 0.8 and $\pm 0.4\%$ strains at zero pressure.

Three evenly-spaced points on the $\omega \leftrightarrow \beta$ pathway (via splitting of the honeycomb layers into alternate $\langle 111 \rangle$ bcc planes) are included for pure titanium. For Ti_3Nb, where the fully transformed ω phase corresponds to $G1$-β as described in Lazar *et al.*[37], three additional points on the energetic barrier identified by Lai *et al.*[39] are included. A mesh of nine evenly-spaced points on the Burgers[40] energy surface of the $\alpha \rightarrow \beta$ transition in pure Ti and $\alpha'' \rightarrow \beta$-$L6_0$ in Ti_3Nb are included.

For defect structures, we include two points on the easy and hard prismatic stacking faults in hcp-Ti. Three points on $\{112\}\langle 111 \rangle$ and one point on $\{110\}\langle 111 \rangle$ faults of bcc-Nb, as well as an unrelaxed vacancy and (100), (110) and (111) free surfaces are included.

Finite temperature structures are included in the database to ensure accuracy in dynamics simulations, including: a 127-atom ab-initio MD snapshot of bcc-Ti containing a vacancy at 1300 K; 432-atom snapshots of Ti_3Nb at (bcc) 300 K, 1000 K and (liquid) 3000 K; a 256-atom snapshot of α'' at 300 K; and snapshots of bcc-Nb at 1200 K, 2200 K and (liquid) 5000 K.

Miscellaneous structures added through the course of fitting and testing for the purpose of improving specific behaviors include α'' Ti_3Nb with b and c scaled by 0.95 and 1.05, lattice constants of bcc-Nb at 50 and 100 GPa, and large-strain (20% and 40%) configurations for C_{44} in niobium. Also included are peaks of the ideal shear curve of bcc Nb at 0 and 100 GPa. Last, configurations of bcc-Ti with a single atom displaced by ± 0.003 Å are included to improve accuracy of force constants in this system.

B. MEAM-like spline-based interatomic potentials for alloys

The embedded-atom (EAM)[22,26] and modified embedded-atom (MEAM)[23–25] methods have been applied to semiconductor elements[20,22–24,26,41] and compounds[42], transition metals[25,43–46] and alloys[47–54]. The original MEAM formalism involves a parametrized analytical functional form which accounts for bond-bending through angular functions with explicit s-, p-, d- and f-orbital characteristics. Lenosky *et al.*[20] first parametrized the MEAM formalism through the use of cubic splines for the study of defects in Si. The use of cubic splines for parameterizing empirical potentials increases model flexibility and efficiency, and has been successfully applied to the study of martensitic transformations in pure titanium[44], shock-loading in niobium[45,55], dislocation dynamics in molybdenum[46] and stabilization of fcc in tungsten at high pressure[56].

The MEAM formalism splits the total energy into pair

and embedding terms:

$$V_{tot} = \frac{1}{2}\sum_{j\neq i}\phi_{IJ}(r_{ij}) + \sum_i U_I(n_i), \tag{1}$$

where the "electronic density" n_i at atom i involves two- and three-body contributions

$$\begin{aligned} n_i = &\sum_{j\neq i}\rho_J(r_{ij}) \\ &+ \sum_{\substack{j>k \\ j\neq i}} f_{IJ}(r_{ij}) f_{IK}(r_{ik}) g_{JIK}(\cos\,\theta_{jik}), \end{aligned} \tag{2}$$

θ_{jik} is the angle of the triplet centered on atom i and the subscript I denotes the atomic species of atom i. Flexibility of empirical MEAM-like potentials for alloys can be adjusted by modifying the atomic species-dependence of the ρ, f and g functions which contribute to the density n. Here we choose a unique f function for each distinct pair of atomic species IJ and a unique g function for each distinct triplet JIK. Since our model for n_i (Eq. 2) is not independent of I, it is not strictly consistent with the Stott-Zaremba[57] corollary to DFT on which the EAM is based and is thus akin to Finnis-Sinclair EAM[58] (FS-EAM) empirical potentials, which assign a pair-index to ρ, interpreted as overlap integrals of neighboring valence wavefunctions. Nonetheless, we herein refer to the fitted potential as MEAM.

C. Genetic algorithm optimization

Development of the optimized potential is an iterative process of fitting, testing, and database refinement. The foremost step in this process is to achieve a balance between database size and the distribution of spline knots to avoid over- or under-fitting. Ten fits are performed simultaneously, and the resultant potentials are tested for accuracy with respect to DFT on a range of properties. The fitting database is refined based on the results of these tests: new structures are added to correct for spurious behavior, or structures are removed when underfitting is suspected. To provide two examples: (1) bcc-Ti phonon structures (via the small displacement method) were added when the L-$\frac{2}{3}$[111] (ω) phonon was found to be inaccurate, and (2) α'' structures strained along the $b-$ and $c-$axes were added when lattice constants were found to vary heavily between fits.

For each individual fit, a global optimization scheme combining a genetic algorithm (GA) with a local downhill optimizer provides a robust method for estimating the optimal parameters. A detailed description of this scheme is provided in Nicklas[59]; here we provide a brief outline.

At each iteration of the genetic algorithm all potentials in a population of ten (distinct from the ten individual fits performed in a "batch") are locally optimized with 60 steps of a Powell[21] conjugate direction algorithm, then the population is sorted and bred according to a weighted least-squares error

$$\mathcal{Z}(\mathbf{y}) = \sum_i W_i^2 \left(Q_i(\mathbf{y}) - Q_i^{DFT}\right)^2. \tag{3}$$

Here, $Q_i(\mathbf{y})$ is an energy, force or stress component computed with the potential specified by parameters $\mathbf{y}$, Q_i^{DFT} is the corresponding DFT value, and W_i is a weighting factor with units to make $\mathcal{Z}$ dimensionless. Units employed are eV, eV/Å and eV/Å^3 for energies, forces and stresses in the database respectively. Weights are $W_{force} = 1\ (\text{eV/Å})^{-1}$, $W_{energy} = 1\ (\text{eV})^{-1}$ and $W_{stress} = \sqrt{2}\,(\text{eV/Å}^3)^{-1}$. Weighting stresses more heavily was found during the course of fitting and testing to produce more reliable elastic constant predictions once a balance of spline knots and database size had been achieved.

Breeding consists of a stochastic combination of spline knots from two parent potentials. The following constraints are enforced by introducing a "punishment" error when not satisfied: (i) $|\max[f_{IJ}(r)]| = 1$ and (ii) n_i lies within the domain of $U_I(n)$ for all i. If the latter constraint is violated, the embedding function is evaluated at its nearest endpoint. At each GA step, for every potential in the population, there is a 30% chance that each embedding function domain and the total density (Eq. 2) are rescaled according to

$$\begin{aligned} U_I(n) &\rightarrow U_I(n/\alpha) \\ n &\rightarrow \alpha n, \end{aligned} \tag{4}$$

where α is determined by the minimum and maximum densities at the current step. During this rescaling, additional symmetries of the three-body terms in Eq. 2 are exploited to keep the maximal value of $f_{IJ}(r)$ fixed at 1:

$$\begin{aligned} f_{IJ}(r_{ij}) &\rightarrow f_{IJ}(r_{ij})/f_{IJ}^{max} \\ f_{IK}(r_{ik}) &\rightarrow f_{IK}(r_{ik})/f_{IK}^{max} \\ g_{JIK}(cos\ \theta_{jik}) &\rightarrow f_{IJ}^{max} f_{IK}^{max} g_{JIK}(\cos\,\theta_{jik}). \end{aligned} \tag{5}$$

While forces and energies are invariant with respect to these transformations, the total error is not because constraints (i) and (ii) are always satisfied after rescaling. Furthermore, spline functions are, in general, not invariant under a transformation of their argument as in Eq. 4. Performing this rescaling thus serves as a genetic mutation to the potential. We also include mutations by, at every GA step, giving each potential a 10% chance of taking a spline knot from a lower-fitness member of the population.

The genetic algorithm is exited when between successive steps the change in total error for each potential in the population is less than 10^{-3}. Parameters for the fitted potential, plots of the functions, descriptions of the fitting algorithms and lists of k-point grids are shown in the Supplemental Material[35].

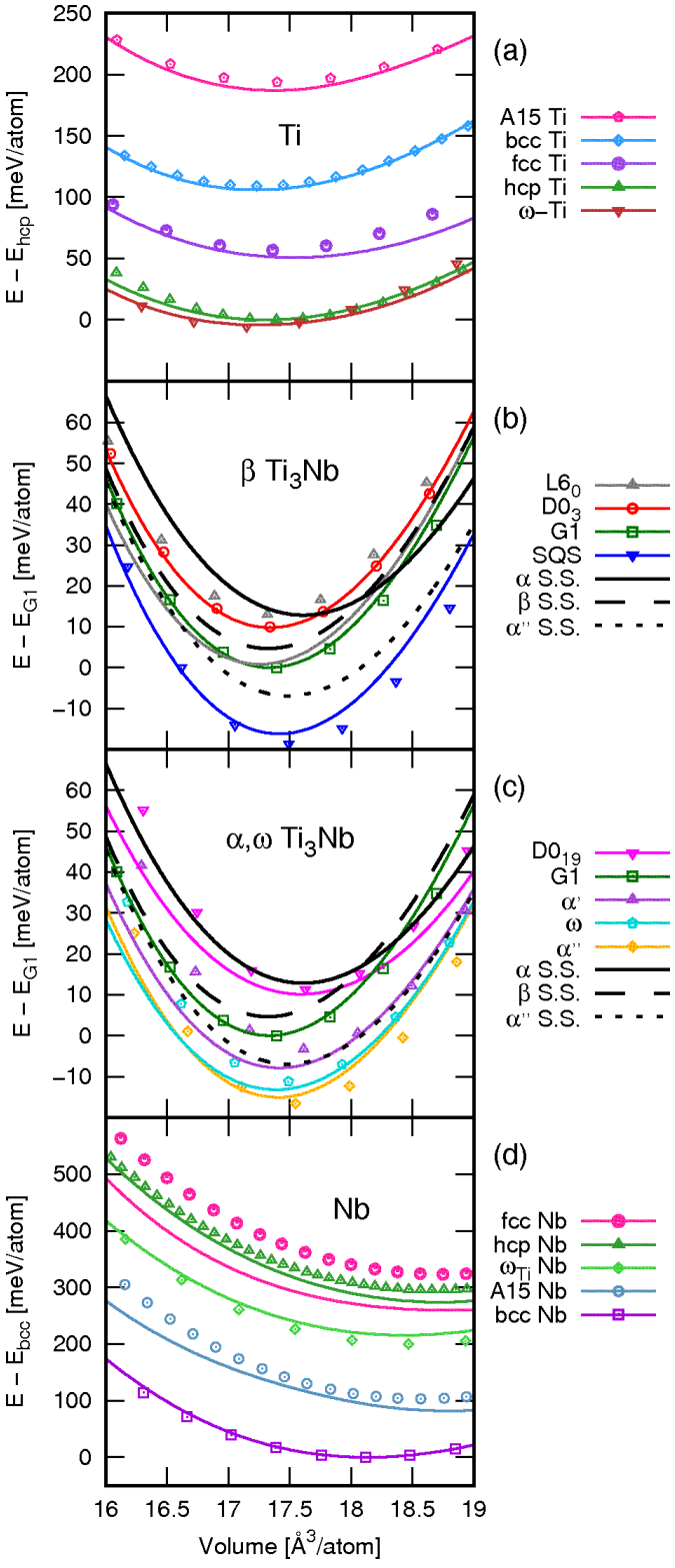

FIG. 1. Energy versus volume curves for (a) Ti, (b) β Ti_3Nb, (c) α and ω Ti_3Nb, and (d) Nb. MEAM values are shown as solid curves, while DFT values are presented as points. Zero energy is defined for (a) as hcp Ti, for (b) and (c) as G1 Ti_3Nb, and for (d) as bcc Nb. Values are given relative to these zeros for the two methods presented. For the Ti_3Nb stoichiometry, fully relaxed solid-solution (S.S.) curves are shown for MEAM.

III. ACCURACY OF THE FITTED MEAM POTENTIAL

We demonstrate the accuracy and transferability of the fitted MEAM potential through the energetics and elastic moduli, crystallographic defects and thermodynamic properties for phases throughout the Ti-Nb phase diagram. All molecular dynamics calculated presented here were performed with the Large-scale Atomic/Molecular Massively Parallel Simulator (LAMMPS)[60] version dated 31 March, 2017. If at any step during an MD run the density seen by an atom exceeds its embedding function domain, the embedding energy is linearly extrapolated from the nearest end point.

A. Structural, Elastic and Thermal Properties

In this section we examine structural, thermal and elastic properties of various Ti-Nb phases with the fitted MEAM potential.

Figure 1 shows energy-volume curves volumetric scaling with fixed lattice ratios, where MEAM energies are shown as curves and DFT energies are points. Figure 1(a) contains energies of pure titanium structures, where MEAM shows excellent agreement with the *ab initio* data, including the nearly degenerate spacing of hcp (α) and ω-Ti. Figures 1(b) and (c) contain structures for bcc (β) and non-bcc Ti_3Nb, respectively. Common bcc intermetallic structures such as $D0_3$ and $L6_0$ are considered, as well as the $G1$ structure proposed by Lazar *et al.*, which contains a chain of niobium atoms along the body diagonal. A fully-relaxed special quasi-random structure (SQS) for the 3:1 ratio in bcc[38] has the lowest energy of all bcc structures, and is slightly lower even than the α'' structure proposed by Sun *et al.*[61]. Solid solution predictions by MEAM are presented as dashed curves. MEAM agrees with DFT predictions of bcc structures with the notable exception of $L6_0$, which can be transformed into α'' by the Burgers[40] mechanism as described in Section IV. In part (c), MEAM shows good agreement with DFT, slightly underestimating the energy of α' and the difference between α'' and ω. Lastly, MEAM again shows good agreement with DFT for pure niobium structures in part (d), except for the energetic ordering of high-lying hcp and fcc Nb. Geometric models of the phases presented here can be found in the Supplemental Material[35].

Figure 2 shows pressure-volume curves for hcp Ti (top) and bcc Nb (bottom) as computed with MEAM and DFT at 0 K, compared with experimental shock data taken from Kinslow[62] at room temperature. MEAM tracks DFT and experiment for bcc Nb, but underestimates hcp-Ti pressure by about 10 GPa at 80% equilibrium volume. The origin of this discrepancy is unclear since DFT agrees well with experiment. Given this anomaly, one must take care when applying the fitted potential to high-pressure phenomena in titanium-rich systems. Below 10 GPa, however, the difference between MEAM and

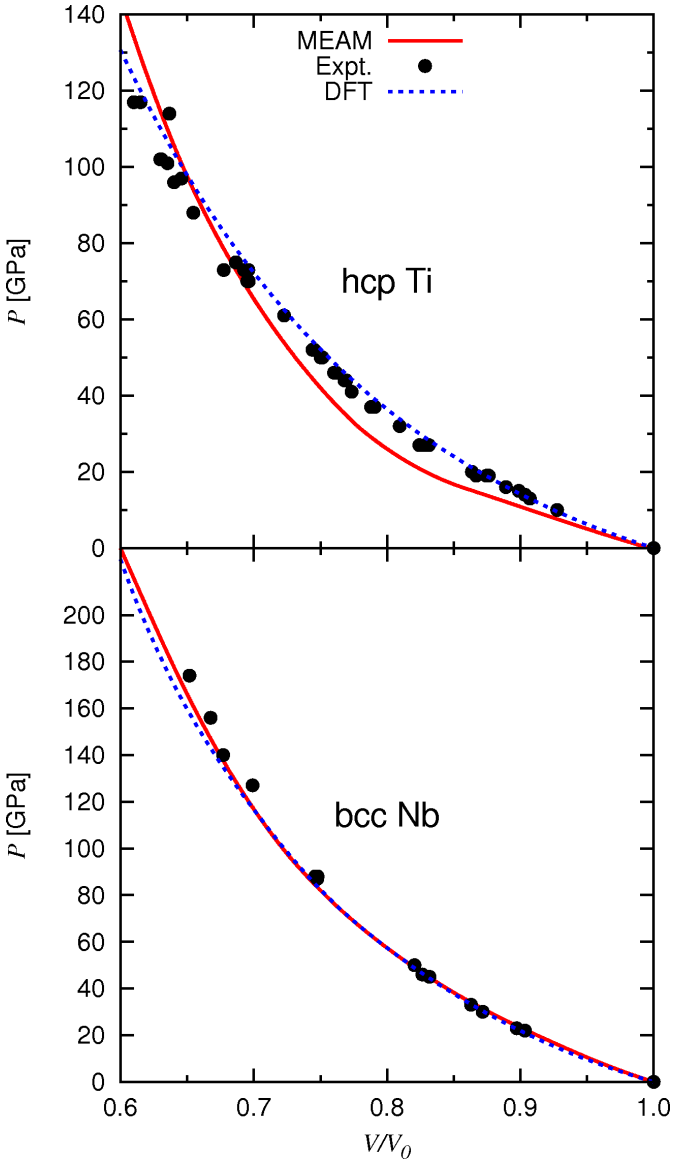

FIG. 2. Pressure-volume relations for hcp-Ti and bcc-Nb. DFT shows good agreement with room-temperature experimental data[62] obtained by shock measurements, but MEAM under-estimates hcp-Ti pressure for compression below $V/V_0 = 0.7$ and over-estimates pressure at higher compression.

DFT is negligible.

Table I displays linear thermal expansion coefficients (TECs) predicted by the fitted MEAM potential and compared with limited experimental data for Ti, Nb, and two alloy stoichiometries. Calculation of the TECs is done using 8,788-atom NPT ensemble simulations with a timestep of 1 fs, where the pressure is kept at zero and the temperature ramped up, starting at RT, over one nanosecond. Every 100 ps, the average temperature and volume over the last 10 ps are computed. The TEC is determined by fitting these to a linear function in the temperature range considered in experiment. MEAM results

TABLE I. Linear thermal expansion coefficients (TECs), in units of 10^{-6} K^{-1}, calculated with MEAM and compared with experiment. MEAM overestimates the TEC at each considered concentration, but shows a decrease with niobium content consistent with experiment.

at. % Nb	MEAM	Expt.
0	11.7	9.50[a], 9.90[b]
2.64	10.9	9.35[a]
11.41	10.8	9.37[a]
100	7.87	7.0[c]

[a]Experimental data for Ti and Ti-Nb from Han *et al.*[63].
[b]Experimental data for Ti from Zinelis *et al.*[64].
[c]Experimental data for Nb from Argent *et al.*[65].

are consistently higher than experimental fits, but the difference shrinks as niobium content increases. Notably, experimental data show a slight increase in TEC between 2.64 and 11.41 at.% Nb, but MEAM values monotonically decrease across the range of niobium content.

Table II contains elastic constants of Ti, Nb, and Ti_3Nb computed in the present work and compared with other *ab initio* and EAM results. Moduli in the present work are calculated using the methodology described by Trinkle[36] using strains of ±0.2%, ±0.4%, ±0.6%, ±0.8%. MEAM matches present DFT calculations to within 20 GPa for most phases, the most notable exceptions being a much softer C_{11} and C_{33} for ω-Ti_3Nb and a negative $C' = (C_{11} - C_{12})/2$ prediced for the $D0_3$ structure. Since the elastic constants of pure ω-Ti are generally softer than those computed for the alloy, it is possible the discrepancy for ω-Ti_3Nb is due to the lack of any strained ω-Ti niobium configurations in the fitting database. Given the solid-solution nature of alloys, however, elastic constants of intermetallic structures do not necessarily give reliable predictions of bulk elasticity.

Figure 3 shows elastic constants of solid-solution bcc Ti-Nb as a function of niobium concentration at 0 K, compared with experiment and previous calculations. Solid lines are MEAM predictions from a 31,250-atom solid solution. To prevent martensite formation and breaking of cubic symmetry, internal relaxations are not allowed. MEAM results are compared with DFT calculations (open symbols) and experimental data for Ti-Nb alloys (filled symbols) as well as gum metals (half-filled symbols). MEAM predicts elastic instability ($C_{12} > C_{11}$) for $x_{Nb} < 10\%$ because the bcc phase is only stable at high temperatures (experimental results for pure Ti from Ledbetter *et al.* are at 1000 °C). The majority of experimental elasticity data for Ti-Nb alloys is between 20 and 40 at.% niobium, where MEAM predictions are accurate. Existing DFT data obtained from various intermetallic structures is also accurate compared to experiment. DFT calculations by Nikonov *et al.*[66] using the effective muffin-tin orbital (EMTO) basis within the coherent potential approximation (CPA) tends to over-estimate C_{44} relative to experiment, particularly in the Ti-rich region.

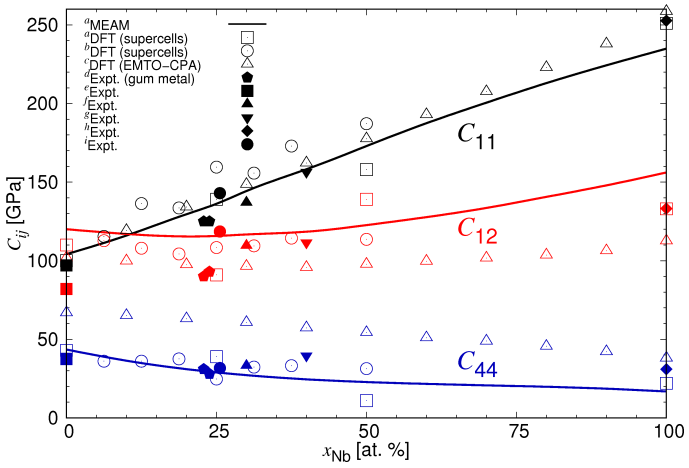

FIG. 3. Elastic constants (in GPa) of bcc Ti-x at.%Nb as a function of niobium concentration x. Solid lines are from a 31,250-atom solid solution as calculated with the fitted MEAM potential using a maximum strain of 0.5%. Open symbols are from DFT calculations of the present work and others, while filled symbols are experimental data. MEAM shows good agreement with experiment across the range of niobium concentration, but in general overestimates C_{12} compared to previous *ab initio* work (open symbols). This gives a smaller value for $C' = (C_{11} - C_{12})/2$, meaning the potential is more elastically anisotropic as measured by the anisotropy ratio $A = C_{44}/C'$.

[a]MEAM and GGA-DFT results of this work.
[b]GGA-DFT results of Karre *et al.*[37].
[c]EMTO-CPA results of Nikonov *et al.*[61].
[d]Two gum metal results of Talling *et al.*[67].
[e]Experimental results of Ledbetter *et al.*[68].
[f]Experimental results of Hermann *et al.*[69].
[g]Experimental results of Reid *et al.*[70].
[h]Experimental results of Carroll[71].
[i]Experimental results of Jeong *et al.*[72].

TABLE II. Single-crystal elastic constants of Ti_3Nb phases by MEAM and DFT compared with data from the literature.

Phase	C_{ij}	MEAM[a]	DFT[a]	DFT[b]	DFT[c]	EAM[d]
hcp Ti	C_{11}	162	172			189
	C_{12}	61	84			74
	C_{13}	68	74			68
	C_{33}	197	190			192
	C_{44}	62	44			50
β-G1	C_{11}	147	142	149		176
	C_{12}	121	112	111		153
	C_{44}	34	34	37		66
β-D0$_3$	C_{11}	115	122	131	117	106
	C_{12}	122	121	119	105	59
	C_{44}	20	19	-8	20	15
ω-G1	C_{11}	169	204	226	162	226
	C_{12}	82	102	117	125	-97
	C_{13}	72	67	81	85	28
	C_{33}	173	250	276	212	212
	C_{44}	30	30	39	19	39
	C_{66}	43	51	55	22	52
α''	C_{11}	122	146	148	130	105
	C_{12}	103	92	93	91	142
	C_{13}	103	124	124	127	115
	C_{22}	183	182	171	148	212
	C_{23}	78	84	80	69	140
	C_{33}	200	176	175	136	149
	C_{44}	53	51	65	28	67
	C_{55}	49	34	45	23	48
	C_{66}	53	69	32	40	62
bcc Nb	C_{11}	235	251			243
	C_{12}	156	133			130
	C_{44}	17	22			28

[a]MEAM and GGA-DFT results of this work.
[b]GGA-DFT results of Lazar *et al.*[37].
[c]GGA-DFT results of Sun *et al.*[61].
[d]Results from EAM Nb-Ti-Al potential of Farkas *et al.*[73]. (calculations by present authors)

B. Planar and Point Defects

In this section we examine behavior of the fitted MEAM potential for point defects and stacking faults in hcp-Ti and bcc-Nb.

Table III contains vacancy and interstitial point defect formation energies for bcc Nb and hcp Ti as calculated in the present work and compared with an existing EAM potential and DFT work from the literature. Present DFT calculations employ 250($\pm$1)-atom supercells while MD calculations use 1,024($\pm$1) atoms. Only vacancy structures are included in the fitting database of the present potential.

Vacancy formation energies of bcc Nb are very consistent between the methods considered here, but the EAM potential of Farkas *et al.* tends to underestimate all interstitial formation energies. We also found that the crowdion configuration collapses with this potential if neighboring atoms are not artificially shifted away from the interstitial atom before relaxation. The present MEAM prediction that octahedral interstitials relax to $\langle 001 \rangle$ dumbbells is consistent with the degenerate energies predicted by Fellinger[76]. MEAM predicts the bcc crowdion to be the energetically favorable contrary to the DFT results, which find $\langle 111 \rangle$ dumbbells to have the lowest energy. However, the *ab initio* energies of these two defects differ by 40 meV in the present work and only 10 meV according to Cerdeira *et al.*[75]. This is unsurprising, given their structural similarity. Indeed, the MEAM prediction of crowdion stability is compatible with the known high mobility of interstitials in non-ferromagnetic bcc metals,[77,78] recently found to result from migration of $\langle 111 \rangle$ defects in tungsten[79].

The fitted MEAM potential tends to overestimate interstitial formation energies in hcp Ti compared to the present DFT calculations, but correctly predicts the BO configuration to have the lowest energy. T and BC configurations are unstable with respect to CS and BO, respec-

TABLE III. Vacancy (Vac.) and self-interstitial formation energies in bcc Nb and hcp Ti. Interstitial configurations for bcc Nb are octahedral (O), tetrahedral (T), crowdion (C), and split (or "dumbbell") structures indicated by angle brackets. Geometry of these defects can be found in Fellinger *et al.*[45]. In addition to O, T and C, basal octahedral (BO), basal tetrahedral (BT), basal crowdion (BC), basal split (BS) and *c*-axis split (CS) configurations are presented for hcp Ti. These geometries can be found in Raji *et al.*[74]. Structures which relax to another interstitial configuration are shown by table entries containing the relaxed structure abbreviation.

	MEAM[a]	DFT[a]	EAM[b]	DFT[c,d]	MEAM[e,f]
			— bcc Nb —		
Vac.	2.74	2.72	2.77	2.67	2.91
O	⟨001⟩	4.89	2.17	5.08	5.27
T	⟨011⟩	4.56	⟨011⟩	4.90	5.38
C	4.73	3.99	⟨111⟩	4.35	4.17
⟨001⟩	5.80	4.76	2.31	5.02	5.27
⟨011⟩	4.88	4.31	2.21	4.65	5.10
⟨111⟩	C	3.95	2.30	4.34	4.16
			— hcp Ti —		
Vac.	2.26	1.38	1.53	1.970	2.26
O	BO	1.57	C	2.13	2.00
T	CS	CS	BS	CS	CS
C	BO	2.16	2.24	2.53	2.30
BO	2.41	1.51	BS	2.25	2.02
BT	BO	3.01	BS	BO	3.69
BC	BO	BO	2.19	BO	BO
BS	2.85	1.87	2.19	2.45	2.22
CS	2.88	1.91	2.78	2.48	2.21

[a]MEAM and GGA-DFT results of this work.
[b]Results from EAM Nb-Ti-Al potential of Farkas *et al.*[73]. (calculations by present authors)
[c]GGA-DFT results for bcc Nb of Cerdeira *et al.*[75].
[d]GGA-DFT results for hcp Ti of Raji *et al.*[74].
[e]Nb MEAM potential of Fellinger[76].
[f]Ti MEAM potential of Hennig *et al.*[44]. (calculations by present authors)

tively, in both methods. We find that the EAM potential of Farkas relaxes many of the interstitials to the BS configuration, which is energetically degenerate with BC despite being structurally distinct after relaxation. We find the present MEAM potential to be consistent with that of Hennig *et al.*[44] for the vacancy formation energy and the instability of T with respect to CS. We note that the formation energies calculated in the present work using the MEAM potential of Hennig *et al.* differ from their published results by as much as 0.64 eV. We suspect this is due to a difference in defect concentrations; their published values correspond to a concentration of about 1% while the present values are for roughly 0.1%.

Figure 4 shows low-index generalized stacking-fault energy (GSFE) curves for (a) hcp-Ti and (b) bcc-Nb. Unrelaxed DFT values are shown as points while MEAM results are shown as solid lines (unrelaxed) and dashed lines (relaxed). For hcp-Ti (a), the $\langle 11\bar{2}0\rangle\{0001\}$ prismatic stacking fault relevant to partial dislocation formation is shown in easy (red) and hard (black) configurations. MEAM predicts a stable partial dislocation as a result of the local minimum at 0.5. Part (b) shows $\{110\}\langle 111\rangle$ (red) and $\{112\}\langle 111\rangle$ (black) GSFE curves for bcc Nb. MEAM predicts a much broader curve for the $\{112\}$ fault than DFT, and reduces energy by about 5 meV/Å^2 upon relaxation. For the $\{110\}$ fault, MEAM tracks DFT quite well and shows a similar reduction in energy of about 5 meV/Å^2 upon relaxation.

In summary, the fitted MEAM potential shows good agreement with existing data on elastic and defect structures near zero pressure. The pressure-volume relation of hcp-Ti (Fig. 2) does not track experiment as well as DFT, but the difference below 10 GPa is negligible. Linear thermal expansion coefficients (Table I) are generally over-estimated but decrease with niobium content in agreement with experiment.

IV. MARTENSITIC TRANSFORMATIONS

Much of the interest in Ti-Nb alloys near the 3:1 stoichiometry comes from their multi-phase nature and martensitic transformations. In this section we examine the energetics of these transitions for intermetallic structures and solid solutions. In the end, an NPT simulation of the shape-memory effect in Ti-25 at.%Nb is performed with the fitted potential.

Figure 5 shows the $\omega \leftrightarrow \beta$ transition pathway for the $G1$ structure in Ti_3Nb and (inset) pure titanium. The reaction coordinate ξ represents a splitting of the sublattices of ω honeycomb planes into bcc $\langle 111\rangle$ planes. The axial ratio c/a is mapped with ξ from the optimal value in ω to the required value in β. The overall lattice constant a is an average of the corresponding values in the endpoint phases. While MEAM overestimates the energetic spacing between ω and β-G1 by 1 eV compared to DFT, a barrier height of about 5 meV/atom from β to ω is predicted by both methods. This is consistent with the work of Lai *et al.*[39], who investigated the energetics of this transformation and the presence of ω at β twin boundaries and $\beta - \alpha''$ interfaces with DFT. The fitted potential also agrees well with present DFT calculations for pure titanium, where the energetic spacing between β and ω is an order of magnitude higher than in the Ti_3Nb system. Since the G1 supercell is but one of many possible chemical decorations of the ω-Ti lattice, we next consider the effect of alloying.

Figure 6 shows the MEAM $\omega \leftrightarrow \beta$ transition at 0 K for multiple niobium concentrations in solid solution, labeled on the curves. The energy of ω is taken as zero, and the right-hand side of the curve represents a complete transition to bcc. This is accomplished by splitting the honeycomb layers of an orthorhombic ω supercell into $\langle 111\rangle_\beta$ planes. At each step, the supercell lattice parameters are relaxed to zero-pressure. The equivalent six-atom

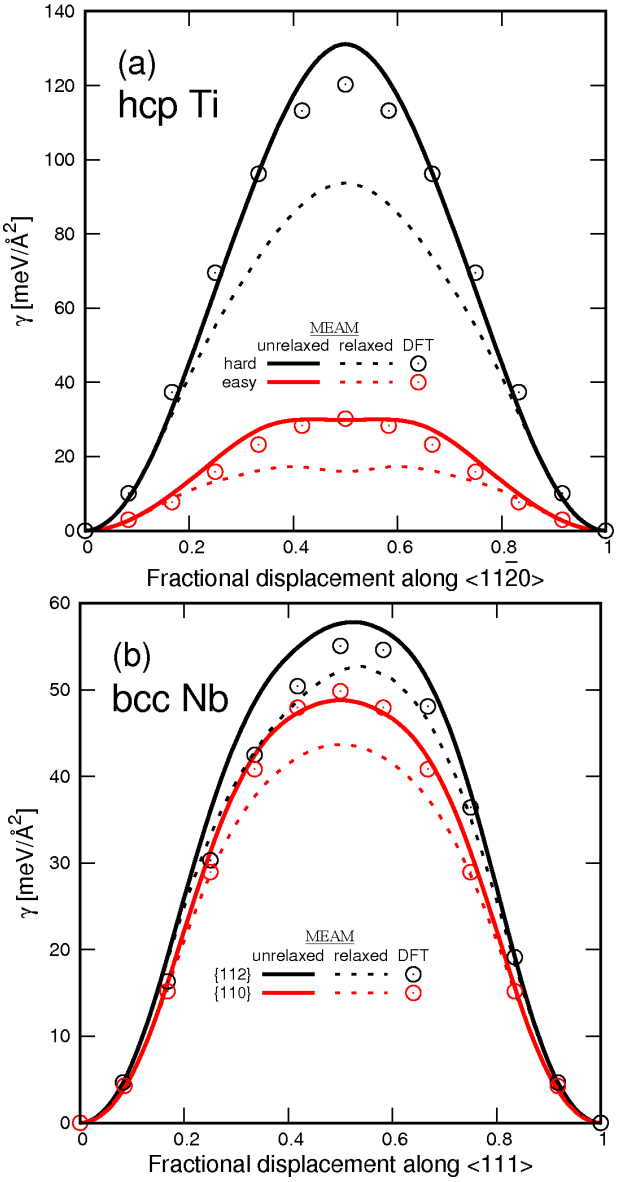

FIG. 4. Low-index stacking faults for (a) hcp Ti and (b) bcc Nb as predicted by MEAM (solid curves) and the present DFT (points) calculations. Faults relaxed with MEAM are shown as dashed curves. Relaxation of the easy prismatic ($\{01\bar{1}0\}\langle 11\bar{2}0\rangle$) fault in hcp titanium reveals a local minimum indicating the formation of partial dislocations consistent with Ghazisaiedi and Trinkle, and Tarrat *et al.*[80,81]. No metastable fault structures are found for niobium.

orthorhombic cell parameters (shown in bottom left) for the lowest-energy structure are plotted in the inset, and curves in the main figure are colored according to the equilibrium structure for that stoichiometry. The fitted MEAM potential does not display a transition barrier from β to ω at any of the considered concentrations, unlike the $G1$ intermetallic transition shown in Figure 5 and that computed by Lai *et al.*[39]. By 30 at.% Nb, the bcc phase is energetically favorable at 0 K. Despite the shift in energy, lattice parameters remain nearly constant due

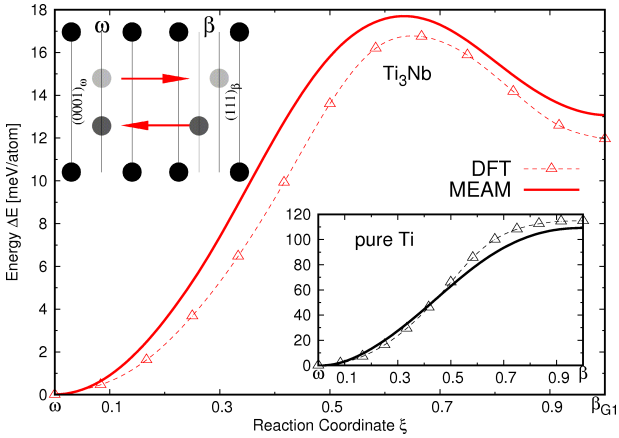

FIG. 5. Transition energy barriers for the ω to β transition in $G1$-Ti_3Nb and (inset) pure Ti via the planar collapse mechanism for MEAM and DFT. The atomic motion during this transition corresponds to a longitudinal 2/3[111] phonon in the bcc lattice as shown schematically in the top left. The c/a ratio is mapped with ξ from the optimal value for ω to the ideal value in β. The overall lattice constant a is an average of the appropriate values in the endpoint phases. MEAM accurately describes the transition in both systems, including the 5 meV/atom DFT barrier from G1-β to ω first identified by Lai *et al.*[39].

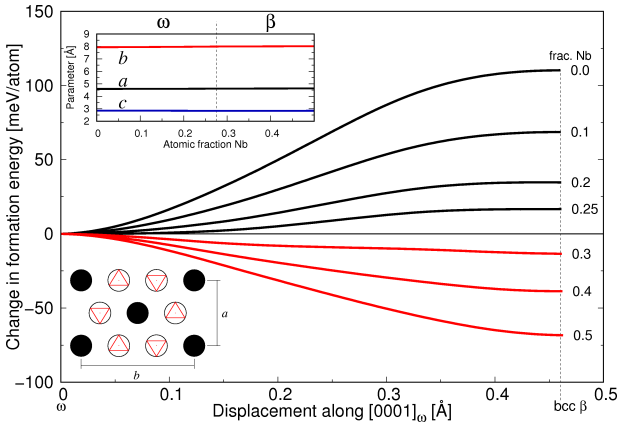

FIG. 6. Evolution of the $\omega \leftrightarrow \beta$ transition pathway at 0 K with niobium in solid solution. A six-atom orthorhombic ω cell is repeated 10×10×5 (3,000 atoms in total) and atomic decoration is randmly assigned to match the niobium concentration shown on the right-hand side of the curves. The horizontal axis represents the displacement as the two 2D-sublattices of the bipartite honeycomb layers are shifted up and down along $[0001]_\omega$, as shown by upward-facing and down-ward facing triangles respectively, until they become different $\langle 111\rangle_\beta$ planes. At each point the cell dimensions are relaxed to zero pressure. The parameters of the lowest-energy structure for each concentration are plotted in the inset. Curves are colored according to the equilibrium structure, where black represents ω-Ti and red represents bcc. The lack of any local minima indicates the potential will not form a trigonal ω phase at equilibrium in any of the considered concentrations. The cell parameters remain relatively unchanged due to the inherent structural compatibility of the β and ω phases.

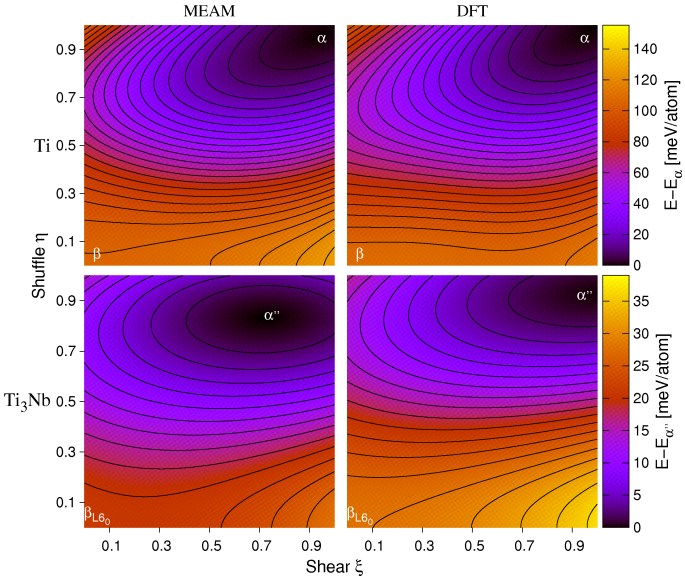

FIG. 7. Potential energy surfaces for the $\alpha \leftrightarrow \beta$ transition by the Burgers mechanism as calculated with MEAM (left) and DFT (right) for pure Ti (top) and Ti_3Nb (bottom). In all cases, $\xi = \eta = 0$ is the location of the bcc β phase ($L6_0$ structure for Ti_3Nb) while α or α'' is located at $\xi = \eta = 1$. Calculations were performed on a 50×50 grid for which η and ξ each vary from -0.125 to 1.125. The energy surfaces are fitted to seventh-order polynomial functions for the purpose of drawing smooth contours.

to the inherent structural compatibility between bcc and ω-Ti. No stable configurations are found at partial transformations, indicating that the trigonal ω phase will not exist in bulk at 0 K with the present MEAM potential. It is worth noting that solutes in beta titanium alloys have been observed to be ejected from the isothermal ω phase into the β matrix upon aging[82,83] but not in quenced ω precipitates where the planar collapse is incomplete[82], so the composition and structure of the ω phase depends heavily on thermal history. The fitted potential should provide a useful tool for atomistic investigation of these effects.

Crystal structure of the α martensite in β-titanium alloys varies with β-stabilizer content. A four-atom orthorhombic cell with space group $Cmcm$ and Wyckoff positions $(0,0,0)$, $(1/2,1/2,0)$, $(0,1-2y,1/2)$ and $(1/2,1/2-2y,1/2)$ can be used to describe β and all variants of the α martensite by changing y and the axial ratios. More detail about this cell is provided in Lazar *et al.*[37]. The Burgers[40] mechanism describing the $\alpha \leftrightarrow \beta$ transition has two independent variables: one which changes the parameter y and another which changes axial ratios. As such, we can obtain potential energy surfaces for $\alpha \leftrightarrow \beta$ and $\alpha'' \leftrightarrow \beta$-$L6_0$ transitions via the Burgers mechanism by tuning this four-atom unit cell.

Figure 7 shows contour plots of energetic surfaces for the $\alpha \leftrightarrow \beta$ transition via the Burgers mechanism. MEAM calculations are shown in the left column, with present DFT work in the right column. Plots on the top row are for pure titanium and plots at the bottom represent a transition from a bcc $L6_0$ structure to the α'' structure proposed by Sun *et al.*[61]. The bcc β structures are located at $\eta = \xi = 0$ and the α and α'' structures are located at $\eta = \xi = 1$. Energies are measured relative to the minimum in each plot.

Shear (ξ) represents simultaneous elongation along $[011]_\beta$ and $[0\bar{1}1]_\beta$, which maps in a linear fashion both the b/a and c/a ratios of the orthorhombic cell from $\sqrt{2}$ to their optimal values in the martensite. Varying the axial ratios with the same parameter is an approximation. EMTO-CPA results of Li *et al.*[84], who examine the optimal relationship between b/a and c/a, indicate that the induced error of the present assumption is on the order of 1 meV/atom for pure Ti. Their results also suggest that the optimal relationship between c/a and b/a becomes more linear with increased niobium content, so this error should decrease.

Shuffle (η) represents a shift of alternating $(011)_\beta$ planes in a $[0\bar{1}1]_\beta$ direction, described by changing y from 1/4 in the bcc lattice ($\eta = 0$) to $y = 1/6$ ($\eta = 1$) in the hcp lattice. In α'', the value of y corresponding to $\eta = 1$ is taken from Sun *et al.* to be $y = 0.2$, but present DFT calculations find an optimal value of $y = 0.204$. Axial ratios corresponding to $\xi = 1$ are the optimal values in the present DFT work. The overall lattice constant a is an average of the appropriate values of the β and martensite lattices.

MEAM and DFT are in good agreement for the burgers transition in pure titanium, and are consistent with the LDA-DFT and EAM results of Masuda-Jindo *et al.*[85].

MEAM underestimates the difference in energy between β-$L6_0$ and α'' as it assigns $L6_0$ an energy about 15 meV/atom lower than DFT. Furthermore, MEAM predicts a α'' phase with incomplete shuffle and shear compared to the DFT structure, indicating a difference in lattice constants and parameter y. Fully relaxed DFT cell parameters of α'' are $a = 3.33$ Å, $b = 4.77$ Å, $c = 4.41$ Å and $y = 0.204$ while MEAM predicts $a = 3.24$ Å, $b = 4.78$ Å, $c = 4.48$ Å and $y = 0.208$. Despite this fitting error, the discussion of Figure 8 shows that the lattice constants of solid-solution α'' predicted by the fitted potential agree well with experiment.

The evolution of martensite phases in β or near-β titanium alloys is important to their morphology and mechanical behavior. The hcp-Ti α phase becomes distorted when alloying with β-stabilizing elements, eventually leading to the α'' orthorhombic phase. This distortion follows the same shuffle mechanism employed in Figure 7, and the position of the minimum-energy state changes with niobium content. We now investigate this deformation in solid-solution Ti-Nb.

Figure 8 reports the MEAM $\alpha \leftrightarrow \beta$ transition energy as a function of displacement in the $[1\bar{1}00]_\alpha$ direction of alternating basal planes $(0002)_\alpha$ for various niobium concentrations (labeled on the curves) at 0 K. At each

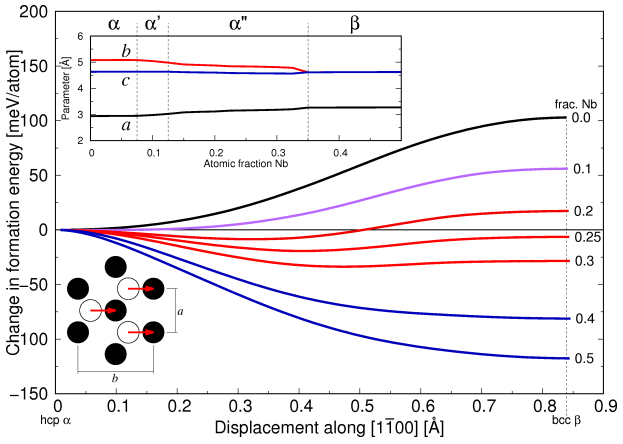

FIG. 8. Evolution of the 0 K equilibrium structure with niobium in solid solution as calculated with MEAM. The four-atom orthorhombic hcp unit cell is repeated 10×10×5 (2,000 total atoms) and atomic decoration is randomly assigned to match the niobium concentration shown on the right-hand side of the curves. The horizontal axis represents displacement in angstroms as alternating basal planes are shifted along $[1\bar{1}00]_\alpha$. The displacement for the completed transformation to bcc is labeled on the right for pure Ti; because the lattice parameter b increases with Nb content, other curves slightly exceed this value. At each point the simulation cell parameters are relaxed to zero pressure. Curves are colored according to the lowest energy structure along the transition path where black is α (hcp), purple is α', red is α'' and blue is β (bcc). Cell dimensions from this structure at 18 concentrations are plotted in the inset with phase boundaries. Only select stoichiometries are plotted in the main figure for clarity. Niobium induces a strain in the hexagonal structure, destabilizing it in favor of α' by ∼7.5 at.% Nb, α'' between ∼12.5 and ∼35 at.% Nb, and bcc beyond 35 at.% Nb.

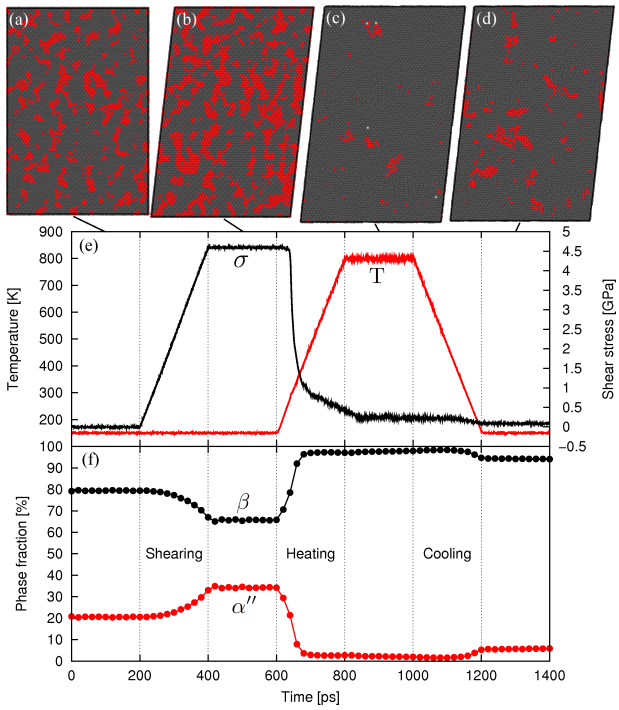

FIG. 9. 364,500-atom NPT simulation of stress- and temperature-induced martensitic transitions in Ti-25 at.%Nb using the fitted MEAM potential with a timestep of 1 fs. (a) shows the cell microstructure at 150 K and 0 GPa with atoms colored by local crystal structure. Grey atoms are identified as bcc and red atoms as α''. (b) shows an increase in α'' martensite upon shearing. (c) shows that a subsequent heating of the cell to 800 K destroys the martensite domains, releasing most of the accumulated shear stress as shown in (e). Martensite domains grow upon cooling (d), but account only for 5.8% of atoms, compared to 20.9% in the pre-cycle structure (f). Structure identification is done by polyhedral template-matching[90] as implemented in the current version of OVITO[91,92].

displacement, the cell is relaxed to zero pressure. The equivalent four-atom orthorhombic cell (bottom left) lattice constants of the lowest-energy structure for 18 concentrations are plotted in the inset. For clarity, only select concentrations are plotted in the main figure. At 10 at.% Nb, no significant minimum develops with respect to the shifting of atomic planes but a slight change in lattice constants a and b indicates a breaking of the perfect hexagonal symmetry, consistent with the formation of an α' martensite phase[86]. With a concentration 20 at.% niobium, a partial displacement of $(0002)_\alpha$ planes is energetically favorable by about 12 meV/atom. This local minimum represents the orthorhombic α'' phase, which is the equilibrium structure up to 35 at.% Nb. Lattice constants of this solid solution α'' structure at 25 at.% Nb are $a = 3.15$ Å, $b = 4.84$ Å and $c = 4.58$ Å, very close the experimental values of $a = 3.19$ Å, $b = 4.80$ Å and $c = 4.64$ Å reported by Sun *et al.*[61]. Beyond 35 at.%, bcc is the lowest energy structure. At this point niobium has completely stabilized the bcc phase as can be see by the lattice parameters where $c = b = a\sqrt{2}$.

The shape-memory effect (SME) is known to exist in binary Ti-Nb alloys[87,88], gum metals[3,6] and other titanium and Ti-Nb alloys[17,86,89]. The SME is characterized by a recovery of initial geometric shape after deformation at a low temperature and subsequent heating. The physical processes that underly this effect are stress- and temperature-induced martensitic phase transitions. Upon straining, a stress-induced transition grows the martensite domains. Subsequent heating of the material induces a reverse transition wherein martensite domains are destroyed and the accumulated stress and strain are recovered. Below, we demonstrate the ability of the fitted MEAM potential to model the stress- and temperature-induced martensitic transitions that underly the SME in Ti-25 at.%Nb.

Figure 9 displays results of a 364,500-atom constant-NPT simulation of stress- and temperature-induced martensitic transitions in Ti-25 at%Nb using the fitted MEAM potential with a timestep of 1 fs. The simulation cell is a 45×45×45 supercell of the four-atom orthorhombic hcp cell. Atoms are assigned chemical species randomly, and the cell is first equilibrated at 150 K and

1 atm pressure. At the top of the figure, cross-sections of the cell are shown at significant points in the simulation. The plane of the page corresponds to $(001)_{\alpha''}$ or $(110)_{\beta}$. Atoms are assigned a color based on local crystal structure as determined by polyhedral template-matching (PTM)[90] as implemented in OVITO[91,92]. Grey atoms are austenite (β) and red atoms are martensite (α''). Note that the PTM method does not distinguish between α, α' or α'', but we refer to the martensite structure as α'' consistent with the stoichiometry used here and the results presented in Figure 8. The middle panel (e) plots shear stress and simulation temperature as functions of time and the bottom panel (f) shows the fraction of atoms identified as martensite and austenite as functions of time.

Between 200 and 400 ps, a shear strain of 5% is applied to the $[100]_{\beta}(0\bar{1}1)_{\beta}$ shear system. As a result, the fraction of atoms in α'' domains increases by 15%. A total of 4.5 GPa of shear stress is accumulated by the cell, and this holds constant between 400 and 600 ps. The simulation cell is heated from 150 K to 800 K between 600 and 800 ps. As can be seen in the bottom panel, martensite domains begin transforming to austenite (bcc) immediately upon heating. By 640 ps, when the temperature is roughly 410 K, the β phase has been saturated at about 95% coinciding with a nearly-complete release of the accumulated shear stress. This gives us an estimate of 410 K for the austenite finish temperature predicted by MEAM, consistent with the experimental value of 390 K reported by Al-Zain *et al.*[88]. Cooling the cell does not cause austenite to revert to martensite until the temperature reaches about 300 K, and the recovered volume fraction of martensite is only 5.8%. This is not a complete cycle of the shape-memory effect but nonetheless demonstrates the ability of the fitted potential to model stress- and temperature-induced martensitic transitions in Ti-25 at.%Nb.

In summary, we have analyzed the $\omega \leftrightarrow \beta$ and $\alpha \leftrightarrow \beta$ transitions in Ti-Nb alloys. The potential was shown to be consistent with present and past DFT calculations, and was used to investigate the effect of alloying on these transitions. The $\omega \leftrightarrow \beta$ transition in solid solution was found to lack the 5 meV/atom barrier present in Figure 5. The α phase was found to distort when alloyed with niobium, first breaking perfect hexagonal symmetry to form α' at $\sim$7.5 at.%, then becoming the orthorhombic α'' phase between $\sim$12.5 and $\sim$35 at.%. The stress- and temperature-induced martensitic transitions between α'' and β that underly the SME in Ti-Nb alloys were demonstrated by NPT simulation.

V. DISLOCATION CORE STRUCTURES

We consider screw dislocations in bcc Nb and hcp Ti and analyze the effect of alloying on the core structure. In both cases we employ a large supercell with periodicity along the dislocation line and fixed boundary condi-

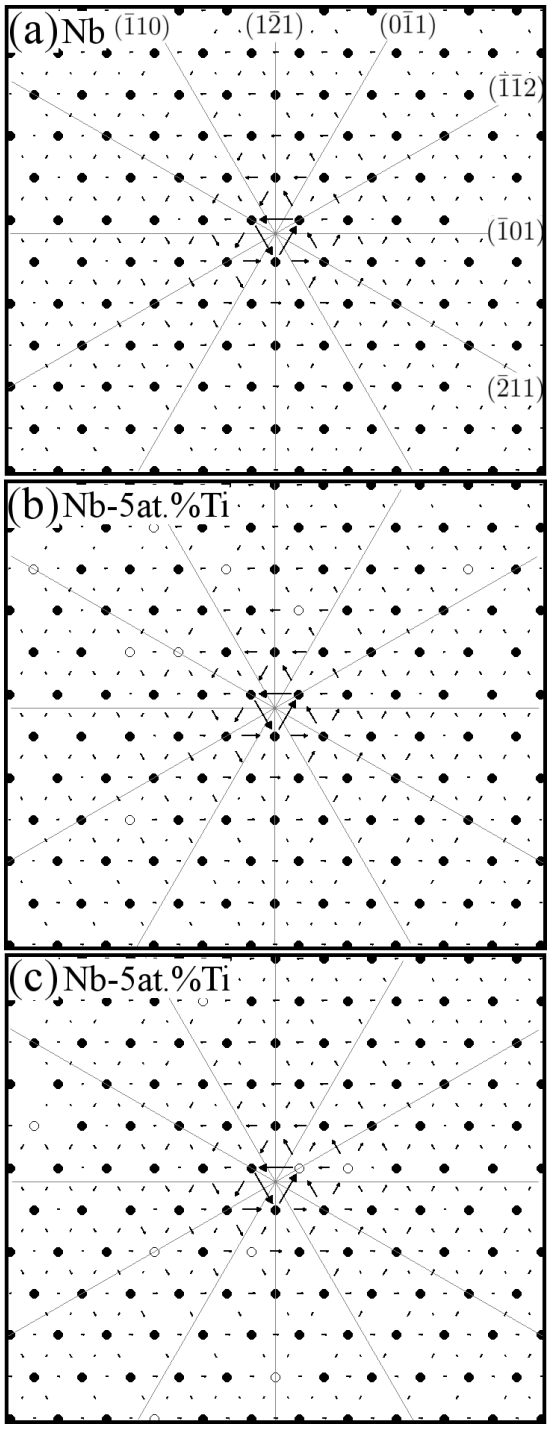

FIG. 10. Core structure of a 1/2[111] screw dislocation in (a) pure niobium and (b) and (c) two configurations of $Nb_{95}Ti_5$. Traces of planes, which are labeled in (a), cross at the origin of the elastic solution. Only screw components (displacements parallel to the burgers vector) are plotted. Niobium atoms are shown in black and titanium atoms are shown in white. MEAM predicts a symmetric core in pure niobium, with little effect on the structure from the presence of titanium solute atoms.

tions in the other two directions. Atoms are displaced in this direction according to the strain field solution from linear elasticity, $u_z = (b/2\pi)\tan^{-1} y/x$, as described in Hirth and Lothe[93]. Fixing atoms at the boundary ensures that the relaxed cell satisfies the long-range boundary conditions imposed by the dislocation. We have employed this method in our previous work on niobium[45], molybdenum[46] and tungsten[56], where more information is available.

Figure 10 contains differential displacement maps of a 1/2[111] screw dislocation in (a) bcc Nb, (b) and (c) two configurations of a bcc Nb-5 at.%Ti alloy. Traces of atomic planes, labeled in part (a), cross at the origin of the elastic solution. The simulation cell has directions $[1\bar{2}1]$, $[\bar{1}01]$, and [111] along x, y, and z repeated 114×190×8 for a total of 1,042,109 atoms with 5 at.% Ti in solid solution. A cylindrical region containing 435,168 atoms, concentric with the dislocation, is relaxed to obtain the core structure. In pure Nb, only a single periodic unit is used along the z direction. MEAM predicts a symmetric core for pure niobium (a), which is found to be very resilient to alloying with Ti in (b) and (c). Even when the titanium solute atom lies on the central triad around the dislocation, as in (c), only slight distortion of the symmetric core is observed. While the six-fold symmetry around the core is broken, the core does not become a three-fold "degenerate" core such as that found for niobium in Fellinger *et al.*[45]. The fitted potential thus predicts titanium solute atoms to have little effect on the slip behavior of bcc niobium.

Figure 11 shows differential displacement maps of a $1/3[1\bar{2}10]$ prismatic dislocation in (a) hcp Ti and (b) and (c) two configurations of an hcp Ti-5 at.%Nb alloy. In these maps, a closed triad of atoms represents a displacement of $b/2$, i.e. a partial dislocation. These triads are shaded in red to guide the eye. Traces of atomic planes, labeled in (a), cross at the origin of the elastic solution. The simulation cell has directions $[\bar{1}100]$, [0001] and $[1\bar{2}10]$ along x, y and z, repeated 155×144×8 for a total of 714,240 atoms with 5 at.% Nb in solid solution. For the dislocation in pure Ti (a), only a single periodic unit is used in the z direction. Of the possible locations for the elastic origin, we place it in the lower energy "mirror" configuration as determined by previous *ab initio* studies[80,81]. A cylindrical region containing 366,912 atoms, concentric with the dislocation, is relaxed to obtain the core structure.

MEAM predicts the dislocation to dissociate in the prismatic plane, separated by an (easy) $\{01\bar{1}0\}\langle 11\bar{2}0\rangle$ stacking fault with symmetry across the basal, consistent with DFT and MEAM results from Ghazisaeidi and Trinkle[80] and DFT results of Tarrat *et al.*[81]. Sub-plots (b) and (c) are different $(1\bar{2}10)$ cross-sections of the same cell, and show significant distortion of the dissociated core structure relative to that in pure titanium. In (b), the presence of Nb atoms near the elastic core causes a spreading into the basal plane. The atoms causing this distortion are the closest solute atoms to the elastic ori-

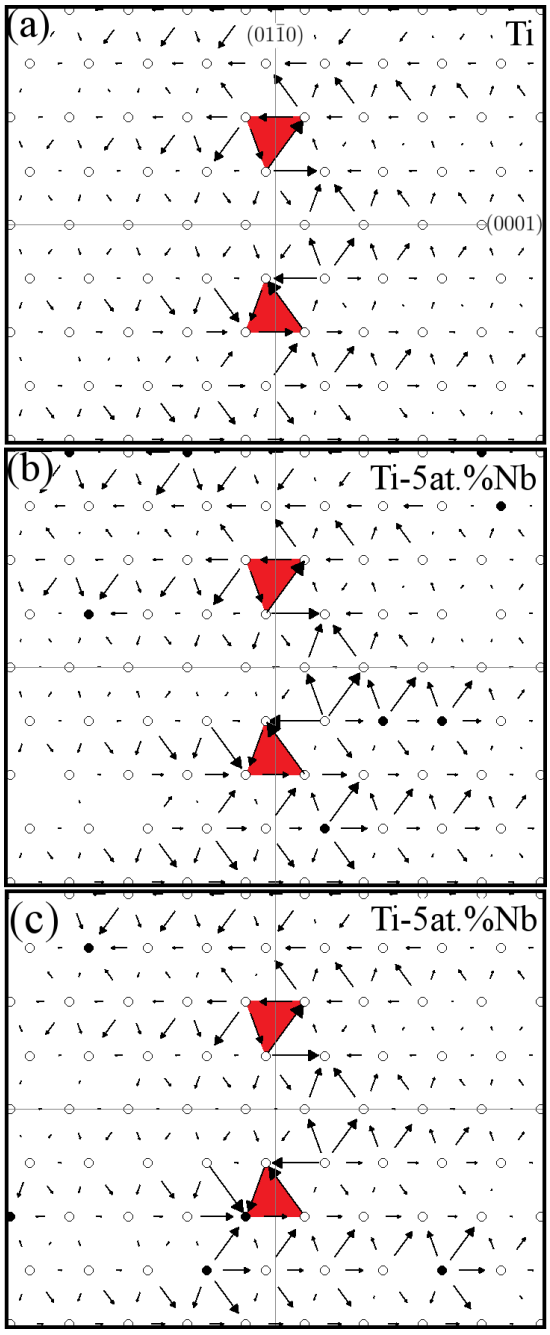

FIG. 11. Core structure of a $1/3[1\bar{1}20]$ screw dislocation in (a) pure titanium and (b) and (c) two configurations of $Ti_{95}Nb_5$. Traces of planes, which are labeled in (a), cross at the origin of the elastic solution. Only screw components (displacements parallel to the burgers vector) are plotted. Partial dislocations are represented by closed triads of atoms, shaded in red to guide the eye. Niobium atoms are shown in black and titanium atoms are shown in white. The structure of this symmetric core is consistent with previous DFT and MEAM calculations by Ghazisaeidi and Trinkle as well as Tarrat *et al.*[80,81]. The presence of Nb near the core breaks the mirror symmetry and causes spreading, primarily into basal planes, but preserves the dissociated structure.

gin, but do not lie on either of the partial dislocation triads. In (c), where niobium atoms are on and near the bottom partial in a pyramidal plane, spreading is less pronounced. Solute atoms appear to have the most significant effect when located near the elastic core on basal planes between the partial dislocations.

The fitted MEAM potential predicts niobium solutes to have a more significant effect on dislocation core structure in titanium than the converse. This is sensible given that hcp Nb is roughly four times higher in formation energy than bcc Ti. The fundamental structure of the dislocations is not affected at 5 at.% solute content in either alloy.

VI. CONCLUSIONS

We present a MEAM-like empirical potential for Ti-Nb alloys, fitted to data across the range of concentrations but focused on martensitic transformations and multiphase properties of gum metal approximants near 25 at.% Nb. The fitted potential is shown to be consistent with previous calculations and measurements of elastic constants, thermal expansion, point defects, stacking faults and martensitic transitions.

We study the impact of alloying on the energetics of martensitic phase transition pathways at 0 K. For the β to ω-Ti transition (Fig. 6), a lack of transition barrier in contrast to the DFT results of Lai *et al.*[39] and the present work (Fig. 5), both of which employed a G1 supercell, is found. The fitted MEAM potential predicts a distortion of the α martensite with niobium content, estimated by calculations along the Burgers transformation pathway (Fig. 8), consistent with experiment. The α'' structure is found to persist in solid solution until 40 at.% Nb at 0 K. Stress- and temperature-induced transitions between β and α'' which underly the shape-memory effect in Ti-25 at.%Nb are demonstrated by NPT simulation (Fig. 9) in a cell with a single β grain.

The effect of solute atoms, with concentrations of 5 at.%, on dislocation cores in hcp-Ti and bcc-Nb is also examined. Symmetric cores of the $\frac{1}{2}\langle 111\rangle$ screw dislocation in bcc-Nb (Fig. 10) are found to be mostly unaffected by titanium solutes, with small amounts of distortion but no significant spreading or change of core structure. The $\frac{1}{3}\langle 1\bar{1}20\rangle$ dislocation in hcp-Ti (Fig. 11), which dissociates in the prismatic plane, is seen to spread primarily into basal planes depending on the location of niobium solutes, but the dissociated structure is preserved.

The fitted potential is suitable for the study of plastic deformation, martensitic transitions, ω-phase formation, defect structures and their interplay in Ti-Nb alloys.

ACKNOWLEDGMENTS

Pure niobium portions of the *ab-initio* database were computed by Dr. Michael R. Fellinger and Dr. Hyoungki Park. Computational resources were provided by the Ohio Supercomputer Center[94]. This work was supported in part by the U.S. Department of Energy under (expired) Contract No. DE-FG02-99ER45795.

[1] T. Saito, T. Furuta, J.-H. Hwang, S. Kuramoto, K. Nishino, N. Suzuki, R. Chen, A. Yamada, K. Ito, Y. Seno, T. Nokana, H. Ikehata, N. Nagasako, C. Iwamoto, Y. Ikuhara, and T. Sakuma, Science **18**, 464 (2003).
[2] Y. L. Hao, S. J. Li, S. Y. Sun, and R. Yang, Mat. Sci. Eng. A **441**, 112 (2006).
[3] H. Y. Kim, Y. Ikehara, J. I. Kim, H. Hosada, and S. Miyazaki, Acta Mater. **54**, 2419 (2006).
[4] S. Kuramoto, T. Furauta, J. Hwang, K. Nishino, and T. Saito, Mat. Sci. Eng. A **442**, 454 (2006).
[5] R. J. Talling, R. J. Dashwood, M. Jackson, and D. Dye, Acta Mater. **57**, 1188 (2009).
[6] H. Y. Kim, H. Satoru, J. H. Kim, H. Hosoda, and S. Miyazaki, Mater. Trans. **45**, 2443 (2004).
[7] X. Tang, T. Ahmed, and H. J. Rack, J. Mater. Sci. **33**, 1805 (2000).
[8] J.-P. Liu, Y.-D. Wang, Y.-L. Hao, Y. Wang, Z.-H. Nie, D. Wang, Y. Ren, Z.-P. Lu, J. Wang, H. Wang, X. H. an dN. Lu, M. J. Kim, and R. Yang, Sci. Rep. **3**, 2156 (2013).
[9] Y. Wang, J. Gao, H. Wu, S. Yang, X. Ding, D. Wang, X. Ren, Y. Wang, X. Song, and J. Gao, Scip. Rep. **4**, 3995 (2014).
[10] M. U. Gutkin, T. Ishizaki, S. Kuramoto, I. A. Ovid'ko, and N. V. Skiba, Int. J. Plast. **24**, 1333 (2008).
[11] Y. Hang, G. P. Li, G. M. Cheng, H. Wang, M. Zhang, F. Xu, and K. Yang, Scripta Mater. **58**, 9 (2008).
[12] Y. Yang, G. P. Li, G. M. Cheng, Y. L. Li, and K. Yang, Appl. Phys. Lett. **94**, 061901 (2009).
[13] H. Xing, J. Sun, Q. Yao, W. Y. Guo, and R. Chen, Appl. Phys. Lett. **92**, 151905 (2008).
[14] E. Plancher, C. C. Tasan, S. Sandloebes, and D. Raabe, Scripta Mater. **68**, 805 (2013).
[15] D. Raabe, B. Sander, M. Friák, D. Ma, and J. Neugebauer, Acta Mater. **55**, 4475 (2007).
[16] M. Friák, W. A. Counts, D. Ma, B. Sander, D. Holec, D. Raabe, and J. Neugebauer, Materials **5**, 1853 (2012).
[17] S. Prokoshkin, V. Brailovski, S. Dubinskiy, Y. Zhukova, V. Sheremetyev, A. Konopatsky, and K. Inaekyan, Shap. Mem. Superelasticity **2**, 130 (2016).
[18] M. Dalstra, G. Denes, and B. Melsen, Orthod. and Craniofac. Res. **3**, 6 (2000).
[19] F. Ercolessi and J. B. Adams, Europhys. Lett. **26**, 583 (1994).
[20] T. J. Lenosky, B. Sadigh, E. Alonso, V. V. Bulatov, T. D. de la Rubia, J. Kim, A. F. Voter, and J. D. Kress, Modelling Simul. Mater. Sci. Eng. **8**, 825 (2000).
[21] M. J. D. Powell, Computer Journal **7**, 2 (1964).
[22] M. S. Daw and M. I. Baskes, Phys. Rev. B **29**, 6443 (1984).
[23] M. I. Baskes, Phys. Rev. Lett. **59**, 2666 (1987).
[24] M. I. Baskes, J. S. Nelson, and A. F. Wright, Phys. Rev. B **40**, 6085 (1989).
[25] M. I. Baskes, Phys. Rev. B **46**, 2727 (1992).
[26] M. S. Daw, S. M. Foiles, and M. I. Baskes, Mater. Sci. Rep. **9**, 251 (1993).
[27] G. Kresse and J. Hafner, Phys. Rev. B **47**, 558 (1993).
[28] G. Kresse and J. Hafner, Phys. Rev. B **49**, 14251 (1994).
[29] G. Kresse and J. Furthmüller, Comput. Mater. Sci. **6**, 15 (1996).
[30] G. Kresse and J. Furthmüller, Phys. Rev. B **54**, 11169 (1996).
[31] P. E. Blöchl, Phys. Rev. B **50**, 17953 (1994).
[32] J. P. Perdew, K. Burke, and M. Ernzerhof, Phys. Rev. Lett. **77**, 3865 (1996).
[33] J. P. Perdew, K. Burke, and M. Ernzerhof, Phys. Rev. Lett. **78**, 1396 (1997).
[34] M. Methfessel and A. T. Paxton, Phys. Rev. B **40**, 3616 (1989).
[35] "See supplemental material at — for a list of k-point grids, DFT lattice constants, descriptions of fitting algorithms and final parameters of the fitted potential.".
[36] D. Trinkle, Scripta Mater. **56**, 273 (2006).
[37] P. Lazar, M. Jahnátek, J. Hafner, N. Nagasako, R. Asahi, C. Blaas-Schenner, M. Stöhr, and R. Podloucky, Phys. Rev. B **84**, 054202 (2011).
[38] C. Jiang, C. Wolverton, J. Sofo, L. Q. Chen, and Z. K. Liu, Phys. Rev. B **69**, 214202 (2004).
[39] M. J. Lai, C. C. Tasan, J. Zhang, B. Grabowski, L. F. Huang, and D. Raabe, Acta Mater. **92**, 55 (2015).
[40] W. G. Burgers, Physica **1**, 561 (1934).
[41] B. Lee, Calphad **31**, 95 (2007).
[42] G. Grochola, S. P. Russo, and I. K. Snook, Chem. Phys. Lett. **493**, 57 (2010).
[43] Y. Mishin, D. Farkas, M. J. Mel, and D. A. Papaconstantopoulos, Phys. Rev. B **59**, 3393 (1999).
[44] R. G. Hennig, T. J. Lenosky, D. R. Trinkle, S. P. Rudin, and J. W. Wilkins, Phys. Rev. B **78**, 054121 (2008).
[45] M. R. Fellinger, H. Park, and J. W. Wilkins, Phys. Rev. B **81**, 144119 (2010).
[46] H. Park, M. R. Fellinger, T. J. Lenosky, W. W. Tipton, D. R. Trinkle, S. P. Rudin, C. Woodward, J. W. Wilkins, and R. G. Hennig, Phys. Rev. B **85**, 214121 (2012).
[47] R. R. Zope and Y. Mishin, Phys. Rev. B **68**, 024102 (2003).
[48] Y. Mishin, Acta Mater. **52**, 1451 (2004).
[49] B. Jelinek, J. Houze, S. Kim, M. F. Horstemeyer, M. I. Baskes, and S. G. Kim, Phys. Rev. B **75**, 054106 (2007).
[50] G. P. P. Pun and Y. Mishin, Philos. Mag. **89**, 3245 (2009).
[51] G. P. P. Pun, V. Yamakov, and Y. Mishin, Modelling Simul. Mater. Sci. Eng. **23**, 065006 (2015).
[52] B. Jelinek, S. Groh, M. F. Horstemeyer, J. Houze, S. G. Kim, G. J. Wagner, A. Moitra, and M. I. Baskes, Phys. Rev. B **85**, 245102 (2012).
[53] G. P. P. Pun and Y. Mishin, J. Phys.: Cond. Mat. **22**, 395403 (2010).
[54] W. S. Ko, B. Grabowski, and J. Neugebauer, Phys. Rev. B **92**, 134107 (2015).
[55] R. F. Zhang, J. Wang, I. J. Beyerlein, and T. C. Germann, Philos. Mag. **91**, 731 (2011).
[56] R. C. Ehemann, J. W. Nicklas, H. Park, and J. W. Wilkins, Phys. Rev. B **95**, 184101 (2017).
[57] M. J. Stott and E. Zaremba, Phys. Rev. B. **22**, 1564 (1980).
[58] M. W. Finnis and J. E. Sinclair, Philos. Mag. **50**, 45 (1984).
[59] J. W. C. Nicklas, *Accurately modelling complex materials*, Ph.D. thesis, The Ohio State University (2013), chapter 5, pages 70-104, `https://etd.ohiolink.edu/pg_10?0::NO:10:P10_ACCESSION_NUM:osu1366210034`.
[60] S. Plimpton, J. Comp. Phys. **117**, 1 (1995).
[61] J. Sun, Q. Yao, H. Xing, and W. Y. Guo, J. Phys. Condens. Matter **19**, 486215 (2007).
[62] R. Kinslow, *High-velocity impact phenomena* (Academic Press, New York, 1970) p. 522.

[63] M.-K. Han, J.-Y. Kim, M.-J. Hwang, H.-J. Song, and Y.-J. Park, Materials **8**, 5986 (2015).
[64] S. Zinelis, A. Tsetsekou, and T. Papadopoulos, J. Prosthet. Dent. **90**, 332 (2003).
[65] B. B. Argent and G. J. C. Milne, J. Less-Common Met. **2**, 154 (1960).
[66] A. Y. Nikonov, A. M. Zharmukhambetova, and A. I. Dmitriev, AIP Conf. Proc **1783**, 020165 (2016).
[67] R. J. Talling, R. J. Dashwood, M. Jackson, S. Kuramoto, and D. Dye, Acta Mater. **59**, 669 (2008).
[68] H. Ledbetter, H. Ogi, S. Kai, S. Kim, and M. Hirao, J. Appl. Phys. **95**, 4642 (2004).
[69] R. Hermann, H. Hermann, M. Calin, B. Büchner, and J. Eckert, Scripta Mater. **66**, 198 (2012).
[70] C. N. Reid, J. L. Routbort, and R. A. Maynard, J. Appl. Phys. **44**, 1398 (1973).
[71] K. J. Carroll, J. Appl. Phys. **36**, 3689 (1965).
[72] H. W. Jeong, Y. S. Yoo, Y. T. Lee, and J. K. Park, J. Appl. Phys **108**, 063515 (2010).
[73] D. Farkas and C. Jones, Modelling Simul. Mater. Sci. Eng. **4**, 23 (1996).
[74] A. T. Raji, S. Scandolo, R. Mazzarello, S. Nsengiyumva, M. Härting, and D. T. Britton, Phil. Mag. **89**, 1629 (2009).
[75] M. A. Cerdeira, S. L. Palacios, C. González, D. Fernández-Pello, and R. Iglesias, J. Nucl. Mater. **478**, 185 (2016).
[76] M. R. Fellinger, *First Principles-Based Interatomic Potentials for Modeling the Body-Centered Cubic Metals V, Nb, Ta, Mo, and W*, Ph.D. thesis, The Ohio State University (2013), chapter 4, page 142, `https://etd.ohiolink.edu/pg_10?115612085608190::NO:10:P10_ETD_SUBID:3564`.
[77] F. Dausinger, J. Fuss, J. Schweikhardt, and H. Shultz, J. Nucl. Mater. **69**, 689 (1978).
[78] H. Shultz, Mater. Sci. Eng. A **141**, 149 (1991).
[79] T. Amino, K. Arakawa, and H. Mori, Sci. Rep. **6**, 26099 (2016).
[80] M. Ghazisaeidi and D. R. Trinkle, Acta Mater. **60**, 1287 (2012).
[81] N. Tarrat, M. Benoit, D. Caillard, L. Ventelon, N. Combe, and J. Morillo, Modell. Simul. Mater. Sci. Eng. **22**, 055016 (2014).
[82] A. Devaraj, S. Nag, R. Srinivasan, R. E. A. Williams, S. Banerjee, R. Banerjee, and H. L. Fraser, Acta Mater. **60**, 596 (2012).
[83] Y. Zheng, T. Alam, R. E. A. Williams, S. Nag, R. Bangerjee, and H. L. Fraser, in *Proceedings of the 13th World Conference on Titanium*, edited by V. Venkatesh, A. L. Pilchak, J. E. Allison, S. Ankem, R. Boyer, J. Christodoulou, H. L. Fraser, M. A. Imam, Y. Kosaka, H. J. Rack, A. Chatterjee, and A. Woodfield (John Wiley & Sons, Inc., Hoboken, NJ, USA, 2016) pp. 59–71.
[84] C.-X. Li, H.-B. Luo, Q.-M. Hu, R. Yang, F.-X. Yin, O. Umezawa, and L. Vitos, Solid State Commun. **159**, 70 (2013).
[85] K. Masuda-Jindo, S. R. Nishitani, and V. VanHung, Phys. Rev. B **70**, 184122 (2004).
[86] G. Lütjering and J. C. Williams, *Titanium* (Springer-Verlag, New York, New York, USA, 2003) p. 341.
[87] Y. W. Chai, H. Y. Kim, H. Hosoda, and S. Miyazaki, Acta Mater. **57**, 4054 (2009).
[88] Y. Al-Zain, H. Y. Kim, H. Hosoda, T. H. Nam, and S. Miyazaki, Acta Mater. **58**, 4212 (2010).
[89] K. Inaekyan, V. Brailovski, S. Prokoshkin, V. Pushin, S. Dubinskiy, and V. Sheremetyev, Mater. Charact. **103**, 65 (2015).
[90] P. M. Larsen, S. Schmidt, and J. Schiøtz, Modell. Simul. Mat. Sci. Eng. **24**, 055007 (2016).
[91] A. Stukowski, Modell. Simul. Mater. Sci. Eng. **18**, 015012 (2010).
[92] A. Stukowski, Modell. Simul. Mater. Sci. Eng. **20**, 045021 (2012).
[93] J. P. Hirth and J. Lothe, *Theory of Dislocations* (Krieger, Malabar, Florida, 1982) p. 60.
[94] O. S. Center, "Ohio supercomputer center," `http://osc.edu/ark:/19495/f5s1ph73` (1987).